In-plane anisotropy of quantum transport in artificial two-dimensional Au lattices

NANO LETTERS
Letter
Cite This: Nano Lett. XXXX, XXX, XXX−XXX
pubs.acs.org/NanoLett

In-plane Anisotropy of Quantum Transport in Artificial Two-dimensional Au Lattices

Kongyi Li,[†,‡] Chunmiao Zhang,[†] Yaping Wu,[*,†] Wenzhi Lin,[†] Xuanli Zheng,[†] Yinghui Zhou,[†] Shiqiang Lu,[†] and Junyong Kang[*,†]

[†]Department of Physics, OSED, Fujian Provincial Key Laboratory of Semiconductors Materials and Applications, Xiamen University, Xiamen 361005, China

[‡]Department of Applied Physics, Eindhoven University of Technology, P.O. Box 513, 5600 MB Eindhoven, The Netherlands

Supporting Information

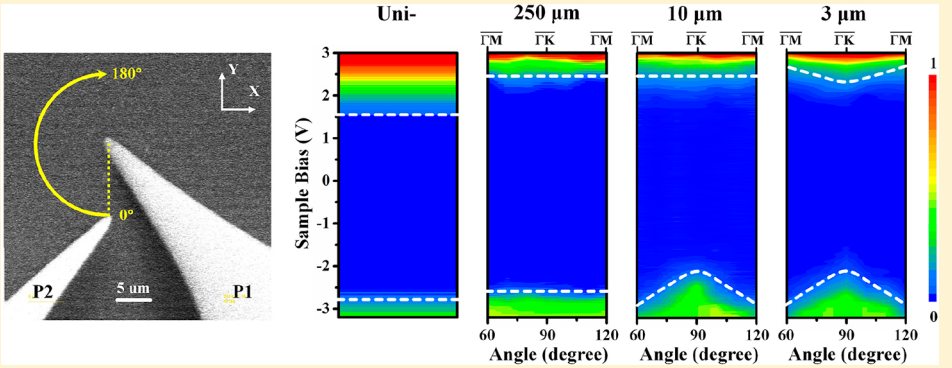

ABSTRACT: We report an experimental observation and direct control of quantum transport in artificial two-dimensional Au lattices. Combining the advanced techniques of low-temperature deposition and newly developed double-probe scanning tunneling spectroscopy, we display a two-dimensional carrier transport and demonstrate a strong in-plane transport modulation in the two-dimensional Au lattices. In well-ordered Au lattices, we observe the carrier transport behavior manifesting as a band-like feature with an energy gap. Furthermore, controlled structural modification performed by constructing coupled "stadiums" enables a transition of system dynamics in the lattices, which in turn establishes tunable resonant transport throughout a wide energy range. Our findings open the possibility of the construction and transport engineering of artificial lattices by the geometrical arrangement of scatterers and quantum chaotic dynamics.

KEYWORDS: *Scanning tunneling microscopy, two-dimensional material, anisotropy, in-plane transport, artificial lattices, quantum chaotic scattering*

Artificial two-dimensional (2D) lattices have become an important subject in condensed matter science and technology due to their advantage of a larger degree of control, which is difficult to achieve in natural nanomaterials (e.g., graphene). Artificial lattices as "quantum simulators"[1] open the possibility of designing, constructing, and tuning the interplay between quantum cooperative effects and tunable parameters (e.g., lattice symmetry, intersite distance, and artificial defects/disorder).[2,3] They offer a platform for comprehending physical phenomena and shedding more light on fundamental physics. When the characteristic length of confinement is close to the Fermi wavelength, a wide range of fascinating phenomena emerge in the system of artificial 2D lattices, such as designer Dirac fermion,[4] tunable topological states,[5] pseudomagnetic quantum Hall effect,[6] Hofstadter's butterfly,[7] Kondo bonds,[8] and magnetic orders.[9] As reported, large-scale artificial 2D Au lattices (2DALs) with honeycomb structure were first constructed, which manifested a novel transport preference and in-plane quantum coupling at room temperature (RT).[10]

Compared with bulk materials, 2D materials have carriers moving in a 2D plane and prevented to move in the third direction, governed by quantum mechanics. Accordingly, the in-plane transport properties of 2D materials become critical, which significantly influences a variety of applications of 2D materials.[11,12] It is essential to have correct tools to fabricate the 2D materials and probe their intrinsic properties, preferably *in situ* tools. At present, one of the most desirable tools to access the "quantum-mechanical world" is a multiprobe scanning tunneling microscope (STM), which combines more than one independently controllable STM-probe with a scanning electron microscope (SEM) in the same ultrahigh vacuum (UHV) and cryogenic environment.[13,14] Together with the complementary navigation of SEM, multiprobe STM with high precision and atomic resolution can provide more degrees of

Received: November 12, 2017
Revised: February 8, 2018
Published: February 12, 2018

DOI: 10.1021/acs.nanolett.7b04783
Nano Lett. XXXX, XXX, XXX−XXX

freedom for *in situ* nanomanipulations and characterizations of individual nanostructures on multiple length-scales. This strategy opens an essential route to reveal the link between structural details and collective phenomena, particularly, quantum transport phenomena in a 2D system.

In this study, to explore the intrinsic transport behavior that is intimately related to the in-plane structure, we implement the low-temperature deposition and double-probe scanning tunneling spectroscopy (STS). A high-quality 2D structure is fabricated, and most of the carriers can be confined to behave as a 2D propagation in the artificial 2DALs. Further investigation of quantum transport is performed with multi-degree-of-freedom measurements and *in situ* controlled modification, allowing us to clarify the underlying transport mechanism and directly control the transport behavior in this 2D system.

Low-Temperature Deposition. As previously reported[10] and also confirmed in our control experiment, 2DALs fabricated at RT are composed of two interfacial distinct layers (denoted as double-layer 2DALs). The consequent interlayer interaction may induce the carrier transport between neighboring layers, thereby leading to a mixture and coupling effect on 2D in-plane transport properties. To exclude the disturbance of interlayer transport and establish a superior 2D platform to clarify the in-plane transport behaviors, we fabricate 2DALs with only a single-layer thickness. It was found that the 2DALs prepared at RT are formed with an Au coverage of 0.8 monolayers (ML), with the two layers growing one after the other via a 2D layer-by-layer growth mode. Subsequently, 3D island growth occurs above (1 ML here is defined as the surface atomic density of Si (111) with an areal density of n = 7.84 atoms nm^{-2}).[15] The growth mechanism can be explained by the Stranski−Krastanov growth mode in which the two layers of 2DALs can be referred to as the wetting layers that follow the registry of the underlying Si (111)−7 × 7 template. Since the wetting condition can be modified by the interlayer interaction between the substrate and wetting layers,[16] the substrate temperature during the deposition can be considered a tunable parameter to weaken the interlayer interaction and reduce the wetting layer thickness (i.e., critical thickness). Accordingly, by optimizing the substrate temperature and Au coverage, completely filled and well-ordered Au lattices with single-layer thickness are successfully fabricated at 200 K (Figure 1a). The Au coverage of 0.4 ML is half of that required at RT (0.8 ML). We, therefore, determine that the critical thickness at this temperature is a single layer. More details of the preparation process at low temperature can be found in the Supporting Information Section 1.

First, STS measurements are carried out with uniprobe STM (the experimental setup of uniprobe STM can be found in Figure S2a in the Supporting Information). As shown in Figure 1b, a uniformly wide gap of about 3.9 eV (from −2.6 to +1.3 eV) is observed in blue curves. Within the gap, detected current is out of the measurable limit of the preamplifier (<5 pA). A similar wide gap obtained at the identical tunneling condition is also seen for the double-layer 2DALs fabricated at RT (i.e., 1.0 eV for the first layer and 4.1 eV for the second layer, shown in Figure S3 in the Supporting Information), which is consistent with the previously reported values.[10] The electronic property of the wide gap that exists only in the second layer is now present in this simplified single-layer system. This phenomenon can be explained by the interactional modulation between the 7 × 7 template and the 2DALs. Low-temperature deposition

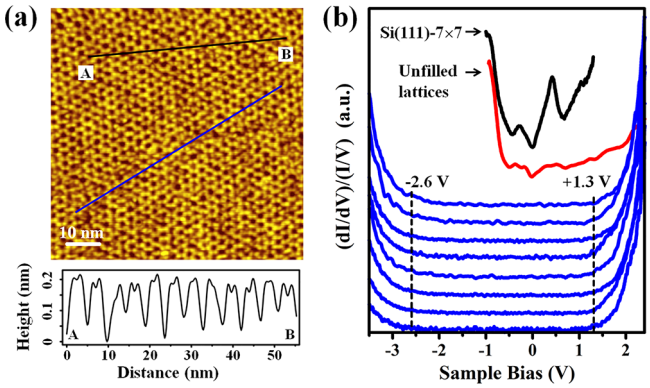

Figure 1. Uniprobe STM image and differential conductance spectra. (a) STM topographic image (70 nm × 70 nm, +3.0 V, 0.1 nA) of 2DALs prepared at 200 K. The lower graph is the height profile along the black line (A to B) drawn in the upper STM image. (b) Normalized differential conductance spectra. The spectra of 2DALs (blue curves) are measured along the blue line in (a), with a set point of +2.5 V and 0.1 nA. Measurements are also taken on an unfilled lattice (red curve) and a bare Si(111)−7 × 7 surface (black curve) with set points of (+2.5 V, 0.1 nA) and (+1.3 V, 0.1 nA), respectively. It exhibits a strong metallic character for the unfilled (imperfect) lattices and a semimetallic character for the 7 × 7 template.

results in a weak chemical bond between Au and Si atoms;[17] thus, electronic transport through the Au−Si interface (as a leakage) is globally suppressed. For the double-layer 2DALs prepared at RT, the Au−Si interplay has a strong interaction in the first layer but a weak interaction in the second layer because of the decay of the interlayer force while it is away from the substrate.[16] Consequently, current leakage at the second layer is notably depressed, and a wide energy gap accordingly emerges in STS, which is equivalent to the manifestation caused by a decrease in the substrate temperature. If we define that the electronic transport in 2DALs is divided into a vertical component and an in-plane component, the wide gap can be attributed to a minimization of leakage (vertical transport) and enhancement of in-plane transport. The latter originates from the quantum coupling effect,[10] while the former can be controlled by decreasing the substrate temperature or increasing the layer stacking. In other words, the measured energy gap of 3.9 eV for single-layer 2DALs (or 4.1 eV for double-layer 2DALs) largely depends on the structure itself, that is, the in-plane arrangement, instead of whichever layer (the first or second layer) that STS is taken on. If we can further suppress the leakage and constrain the current to 2D propagation over the surface, then more detailed characters of carrier transport that are intimately related to the structure with in-plane arrangement are supposed to appear.

Double-Probe STM/STS. Although the vertical electronic transport has been globally suppressed, its influence cannot be excluded in the above-mentioned scheme. Thus, in order to restrict the injected current to 2D propagation and protect the Au lattices beneath the tip as well, we develop a new method for noninvasive transport measurement with double-probe STM/STS (more discussion can be found in the Supporting Information Section 2). As shown in Figure 2a, Probe 1 is in contact with the 2DALs via an external z-height control, thereby preventing serious surface damage. Probe 2 (non-contact tip) is controlled by the STM control system and performs STM imaging or spectroscopy. The bias voltage is applied via Probe 1 instead of the back of the Si substrate; thus,

DOI: 10.1021/acs.nanolett.7b04783
Nano Lett. XXXX, XXX, XXX−XXX

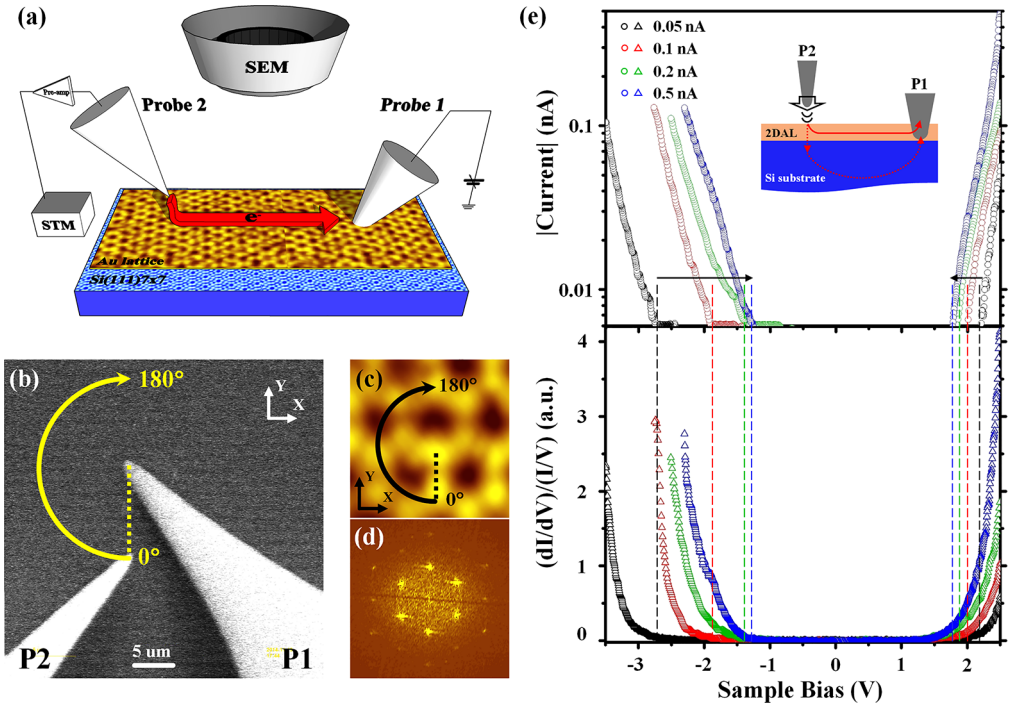

Figure 2. Configuration of double-probe STM. (a) Schematic of the experimental setup of the double-probe STM/STS in this work. Probe 1 is in contact with the 2DALs and applies bias voltage; Probe 2 is controlled by STM electronics and establishes a tunneling junction. The injected current (red arrow) arriving at the 2DALs surface is drawn toward Probe 1 by a surface electric field. Both probes can be navigated and positioned under SEM. (b) SEM image of double-probe STM/STS on 2DALs (top view). The tip−tip spacing is kept constant, whereas the Probe 2 (P2) is actuated around the Probe 1 (P1) from 0° to 180° (azimuthal angle). (c) Rotation of the azimuthal angle with respect to the real lattices in 7 nm × 7 nm STM imaging (thermal drift has been calibrated). (d) Fourier transform of the STM topographic image in Figure 1a. (e) Tip-height dependent $I-V$ curves (upper) and corresponding dI/dV spectra (lower) obtained at a fixed voltage of +2.5 V and various set point currents of 0.05, 0.1, 0.2, and 0.5 nA. The vertical colored dash lines indicate the onsets of the tunneling current of each $I-V$ curve. All the measurements were performed at an identical $x-y$ position with a 10 μm tip−tip spacing.

the injected current from Probe 2 is laterally yielded by the surface electric field and then propagates toward Probe 1 along the surface. In this scheme, vertical transport is largely suppressed, and the intrinsic features of electronic transport in 2DALs can be further explored. With the SEM navigation, the probe spacing and the relative positions are well controlled, further enabling an angle-dependent and a distance-dependent transport measurement. Figure 2b displays the operation of double-probe STM in the SEM monitor. Probe 1 at the center is in contact with the 2DALs; Probe 2 rotates from 0° to 180° (azimuthal angle) around Probe 1 and proceeds STS measurements every 10° with a constant separation of 10 μm. Given that both STM and SEM imaging share the same $x-y$ coordinate, the corresponding rotation in the real lattices can be determined (Figure 2c). Figure 2d gives the Fourier transform of a typical STM topographic image. The pattern of reciprocal lattices shows a 6-fold symmetry, thereby implying that the 2DALs have hexagonal 2D Brillouin zones. Accordingly, the azimuthal angles in real space can correspond to the specific directions in the first Brillouin zone.

Since one of our STM tips is operated in an STS mode, a tunneling barrier is inevitably involved in the double-probe measurement. In order to identify the influence of this tunneling barrier as well as any possible background leakage through the substrate and interface, a sequence of $I-V$ curves with different tip−sample separations are measured (Figure 2e). Different tip−sample separations are controlled by holding the tip at an identical $x-y$ position and adjusting the set point current and bias voltage. With the tip approaching the sample surface (corresponding to the set point current increasing from 0.05 to 0.5 nA), the energy gap shrinks to $E_{g(0.5\ nA)}$ = 3.1 eV (from −1.3 to +1.8 eV). A further tip approach results in a jump to point contact with an abrupt current increase exceeding the preamplifier current limit. Given that no apparent surface electronic state has been detected around the current onsets all over the surface, we estimate that the intrinsic energy gap of the 2DALs is about 3.1 ± 0.1 eV. Within the gap, STM imaging becomes very unstable, owing to a series of point contacts occurring between the tip apex and the sample surface.

We also notice an interesting feature in Figure 2e that the current onset at the positive bias shifts more slowly than that at the negative side. This polarity-dependent behavior can be attributed to a tip-induced ballistic electron injection.[18] As illustrated in the inset of Figure 2e, at a high positive bias, the ballistic electrons emitted from Probe 2 penetrate into the bulk substrate, providing a leakage current that is not modulated by the surface 2DALs. Simulation of current density distribution from one tip to the other also confirms the existence of this ballistic leakage (shown in Figure S4 in the Supporting Information). These leaking hot electrons enhance the collected current and render the transport current less sensitive to the propagation direction. When switching to a negative bias, this effect is largely suppressed.

In order to ensure the comparability and focus on intrinsic transport behaviors in the 2DALs, the tip−sample separation is fixed. Besides, even if the tip−sample separation can be adjusted to a small enough value to determine the intrinsic energy gap, tip-field-induced material transfer (from the surface

DOI: 10.1021/acs.nanolett.7b04783
Nano Lett. XXXX, XXX, XXX−XXX

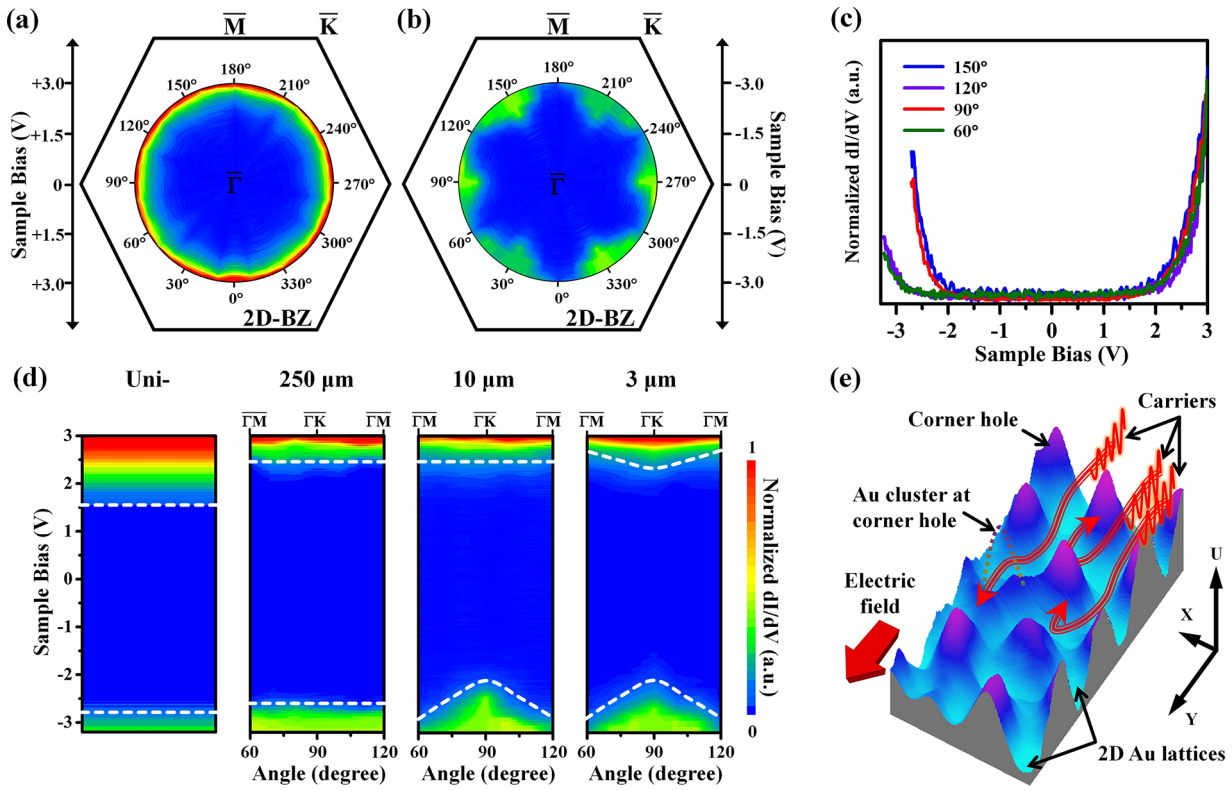

Figure 3. Double-probe STS characterizations. Angle dependence of STS measured with 10 μm tip−tip separation at (a) positive and (b) negative bias, ranging from 0 to ±3.0 V, respectively. The radius represents the sample bias voltage; the colors from blue to red represent the increase in the differential conductance in 2DALs. The surrounding hexagon represents a 2D Brillouin zone (2D-BZ). Limited by the motion range of Probe 2, measurements cannot be extended to another semicircle (right side of Probe 1) in one experiment. The data shown with the angles from 190° to 350° are copied from the results on the opposite side for a better illustration. These data are verified to have similar features, after replacement with a new tip and changing to a clean area. (c) Four STS spectra measured along four typical azimuthal angles with the same tip−tip separation of 10 μm. (d) Angle-dependent STS with tip−tip spacings of 250, 10, and 3 μm. For comparison, the result of uniprobe STS is drawn in the "Uni-" panel without angular variation. The dashed lines (guides for visualization only) mark the onsets of differential conductance. All the dI/dV spectra are recorded under the identical tunneling condition of +2.5 V and 0.1 nA and with the same color scale. (e) Schematic of carrier motion in an energy landscape (as in the barriers array). The corner-hole vacancies function as hard barriers (purple hills) and the Au lattices act as conductive conduits (light blue region). As indicated by the red trajectories, carriers under a surface electric field undergo elastic and inelastic scatterings when they encounter barriers but pass or tunnel through them when the barriers are dressed with Au clusters.

adatoms or tip atoms) at such a distance range happens all the time. We, therefore, retract the tip to a safe height (corresponding to the set point of 0.1 nA and +2.5 V) in all the following angle-dependent and distance-dependent STS tests. It will consequently introduce a large tunneling resistance, taking about 80% of the electrical potential drop at the low bias region. However, since the tunneling resistance only affects the transmission coefficient of tunneling current and the sensitivity of current measurement, it will not introduce any transport anisotropy or change the energy position of detected states.

Band-like Transport in Well-ordered 2DALs. The angle-dependent STS results with a 10 μm tip−tip separation are shown in Figure 3a,b in polar coordinates. At a small bias range, no current signal has been detected (blue region), which is consistent with the results of uniprobe STS. As the strength of the electric field increases, carrier propagation through the whole lattice is allowed. However, the angular distributions exhibit a large difference between the positive and negative bias ranges. At the positive bias, carrier propagation presents a nearly uniform distribution (Figure 3a), whereas at the negative bias, the threshold energy of carrier propagation varies with the azimuthal angles, showing a 6-fold symmetry (Figure 3b). Figure 3c gives four typical STS spectra measured along the azimuthal angles of 60°, 90°, 120°, and 150°, in which the repeating of differential conductance can be clearly seen. Since the tunneling condition in all the measurements is identical, tunneling resistance is keeping the same and cannot lead to any conductance anisotropy. A similar double-probe STS is also performed to identify a possible influence of the underlying 7 × 7 template. The result shows no difference between single-probe and double-probe STS spectra and no hint of in-plane anisotropy on Si(111)−7 × 7 surface. It means that the anisotropy of the in-plane carrier transport should be caused by the 2DALs itself.

Considering the characteristic length in this system, for example, the lattice constant (~2.69 nm) is five times the Fermi wavelength in Au (~0.5 nm),[19] a tentative explanation for carrier motion in 2DALs is given as follows. For electronic transport, corner holes in the 2DALs function as hard scatterers because of missing Au atoms (showing vacancies), while Au lattices function as a conductive atomic network because of the quantum coupling effect[10] between neighboring Au clusters. As shown in Figure 3e, in a potential landscape, a carrier travel over the 2DALs can be considered as carrier motion in a periodic barrier array, where the carrier functions as a wave packet that undergoes intensive elastic and inelastic scattering

DOI: 10.1021/acs.nanolett.7b04783
Nano Lett. XXXX, XXX, XXX−XXX

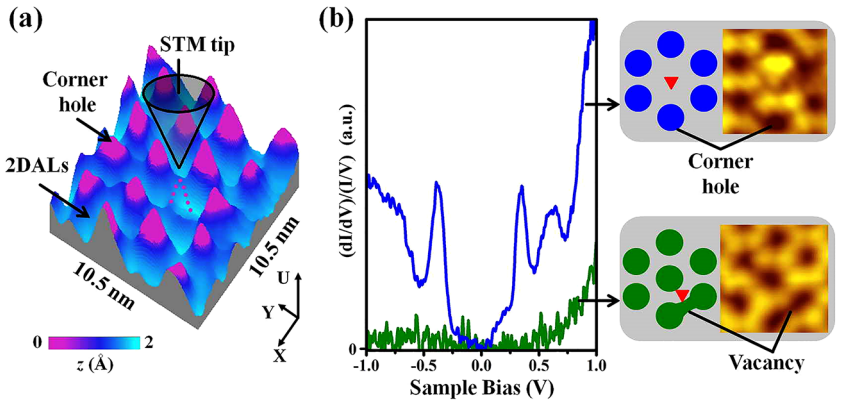

Figure 4. Local structural modifications and resulting differential conductance. (a) STM image of the stadium plotted in a 3D view, where the vertical axis schematically indicates the energy height (U) and the color indicates the morphology in real lattices. Individual barrier beneath the STM tip apex is eliminated by embedding an Au cluster into corner-hole vacancy via tip manipulation. (b) Uniprobe STS spectra obtained at the center of the stadium (blue) and on the asymmetric array (green). Set point: +2 V, 0.1 nA. The right panels with STM images and corresponding schematics indicate the probed local structures. The disks represent the corner holes. The "vacancy" denotes a ditch between two neighboring corner-hole vacancies, which changes the array into asymmetry. The red triangles inside denote the positions of the STS taken on.

during propagation.[20,21] In a long-range, such barriers with non-negligible diameter are arrayed in a hexagonal pattern that resembles a quantum Lorentz gas system.[22−26] When a small electric field is applied, the carrier motion in the barrier array as a diffusion along the field direction is strongly chaotic and ergodic, which manifests itself as being blocked and trapped, thereby leading to an extremely low conductance (i.e., the energy gap in the spectrum). With the increasing strength of the electric field, the ergodicity (or hyperbolic property) is gradually lost,[23] and the escape probability of the carrier increases to a sufficiently high value that can be detected by the current preamplifier, which corresponds to the current onset in the spectrum. In the reciprocal space, the anisotropic distribution can be viewed as a carrier traveling in the 2DALs, which behaves as a superdiffusion[27] along the $\bar{\Gamma}-\bar{K}$ direction while undergoing a serious block along the $\bar{\Gamma}-\bar{M}$ direction. The injected carrier passing through the 2DALs (the scatterer array) behaves as though it is propagating in a transport band structure. Such band-like carrier transport is universally determined by the dynamics of carrier motion (quantum chaotic dynamics) and lattice symmetry (honeycomb structure here).[28] Similar phenomena have already been demonstrated in other systems, such as coupled quantum dots,[29,30] moiré superlattices,[7] and molecular gate array.[4] At the same time, we realize that this transport anisotropy can also be referred to as a nonlinear behavior, i.e., the current vector is not parallel or noncolinear to the field vector and will contribute a transverse current component to the in-plane transport. A conductivity coefficient containing higher rank of tensors may be another way of understanding the band-like transport observed in the 2DALs.

Given the 6-fold symmetry mentioned above, we concentrate only on the azimuth from 60° to 120°. Due to the disturbance of the ballistic leakage current, the anisotropy of carrier transport at the positive bias is invisible at 10 μm tip−tip spacing ("10 μm" panel in Figure 3d). When the spacing reduces to 3 μm, the surface current is enhanced. The anisotropy becomes obvious at both the positive and negative bias ranges ("3 μm" panel in Figure 3d). When the propagation distance increases to 250 μm, the transport band caused by quantum chaos is gradually lost, and the breakdown of the anisotropy progressively occurs ("250 μm" panel in Figure 3d). On one hand, the extension of tip−tip distance increases the leakage current through the Si substrate and correspondingly reduces the surface current sensitive to the propagation direction. On the other hand, a longer propagation distance increases the step-edge scattering, which could be another reason for the coherence loss.[31]

Compared with the spectra examined by uniprobe STS with the identical tunneling condition ("Uni-" panel in Figure 3d), the gap observed by double-probe STS (ranging from +2.2 to −2.5 V around) slightly increases and shows a better symmetric feature with respect to the Fermi level. Given that the Si substrate we used is highly *p*-doped, the asymmetric feature in uniprobe STS mainly and inevitably arises from the electronic structure of the underlying Si template due to its uniprobe configuration. On the contrary, in the double-probe configuration, the injected current is drawn to the lateral direction and largely restricted within the 2DALs surface. The differential conductance, therefore, is strongly modulated by the 2DALs. The vertical transport, which we refer to as leakage through the whole Si substrate, is largely suppressed. Thus, the gap further enlarges and the symmetry is improved with respect to the Fermi level.

Tunable Resonant Transport in Modified 2DALs. Given the periodic and compact arrangement of scatterers and the long-range interaction[24] among carriers, carrier motion in the 2DALs under a small surface electric field is strongly chaotic, i.e., the dynamics is hyperbolic chaos.[23,25] The resulting differential conductance spectrum exhibits a wide gap and a monotonic rise of conductance at the edges. To a large extent, the geometry of this array plays a decisive role in the chaotic dynamics of carrier motion and the formation of band-like transport. What if we perform a structural modification that locally changes the scatterer arrangement? Driven by this, we tentatively erase an individual scatterer via the atomic manipulation upon well-ordered 2DALs, by which an Au cluster is dedicatedly embedded in the corner-hole vacancy. Therefore, a tiny "stadium" surrounded by outer barriers is formed (Figure 4a). Given that the stadium size should be larger than or comparable to a critical length of ∼2 nm if electron confinement is expected,[29] the removal of the scatterer implies that the spatial spacing gives sufficient room for constructing local electronic resonance. Besides, the resonance

DOI: 10.1021/acs.nanolett.7b04783
Nano Lett. XXXX, XXX, XXX−XXX

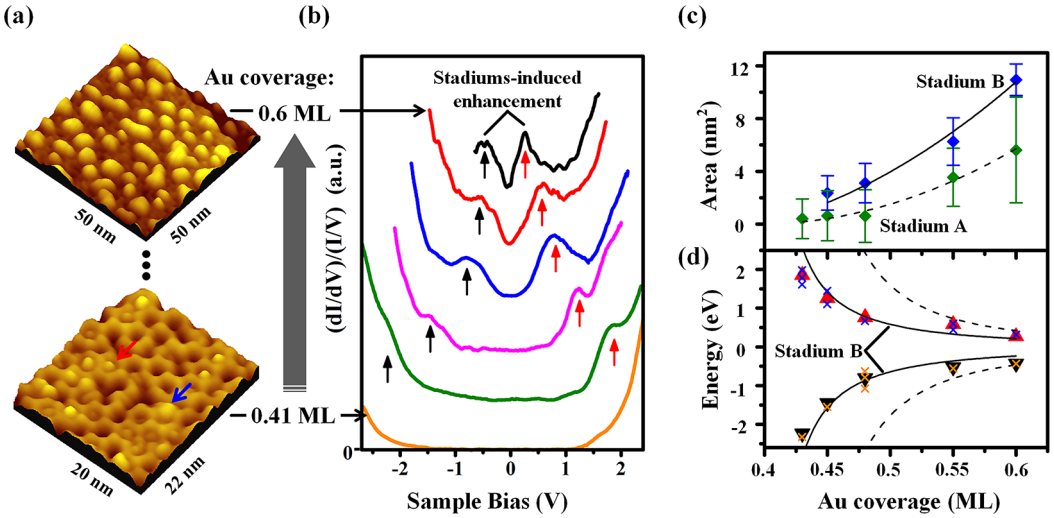

Figure 5. Global structural modifications and resulting differential conductance. (a) STM topographic images of 0.6 and 0.41 ML Au coverage with a set point of +2.5 V and 0.1 nA. The blue and red arrow indicate the exceeded clusters decorated on Au lattices and at corner-hole sites, respectively. (b) Series of differential conductance spectra with the evolution of Au coverage from 0.41 to 0.6 ML (set point: +2.5 V, 0.1 nA). The peaks of conductance enhancement are indicated by the black and red arrows originating from the hole and electron resonance, respectively, as induced by stadium B. (c) Size statistic of Au islands with an evolution of Au coverage. The distribution of each kind of stadium (blue square for "A" and green square for "B") is fitted by Gaussian statistics (the error bar denotes the fwhm). The dashed curves (for stadium A) and solid curves (for stadium B) show the fitting results. (d) Black and red triangles represent the positions of the hole and electron resonant peaks, respectively, as shown in (c). The fitting results show that the energy positions well match the evolution of resonant states formed in stadium B (solid curve) rather than in stadium A (dashed curve). The crosses represent the positions of the resonant peaks that emerge only at the positive (blue) or negative (yellow) bias side in some cases.

suppression electronically induced by the scatterer at the stadium center is removed.[32] The resulting redistribution of electronic conductance can be clearly seen in the uniprobe STS spectrum, characterized by several resonant peaks (blue curve in Figure 4b) around the Fermi level. This local resonance, as in a loosely arrayed "quantum corral",[20] is constructed by the confinement of outer barriers round by round, thereby suggesting the formation of periodic stable orbits instead of hyperbolic chaos in the stadium. If we create an additional scatterer by removing a local Au cluster, the symmetry of the scatterer arrangement is broken, such that the resonant orbits cannot be observed (green curve in Figure 4b) and the carrier motion reverts to strong chaos. These results suggest that a geometrical arrangement of stadiums can alter the inner carrier dynamics. If the range of structural modifications can be extended further, e.g., building a series of coupled stadiums on a large scale, the long-range transport behavior in the 2DALs is expected to be modified.

As mentioned above, an Au coverage larger than 0.4 ML results in the formation of 3D Au islands on well-ordered 2DALs, which can also function as scatterer "erasers" to some extent. Unlike the embedded cluster manipulated by the STM-tip, a deposited Au island can once fill two or three corner-hole vacancies and build a large stadium. Such a large size and number of stadiums strongly modulate the global carrier transport. Carrier motion is expected to be routed from hyperbolic to nonhyperbolic chaos,[33,34] thereby leading to an emergence of stable orbits [i.e., Kolmogorov–Arnold–Moser (KAM) tori] as in an individual stadium, or at least a behavior with a minimum Lyapunov exponent.[35] These stable orbits not only can easily be detected but also make a dominant contribution to carrier transport at certain energy [i.e., changing from KAM to non-KAM dynamics].[36−38] Given the construction of stadiums lies on the Au islands, the implemented transport control can be simplified as the controlled growth of the Au islands.

To corroborate the speculation, we perform a structural modification by gradually increasing the Au exposure. Transport measurements are carried out under the scheme of double-probe STM/STS with 3 μm tip−tip separation. As shown in Figure 5a, under the coverage of 0.41 ML, the exceeded Au clusters cannot follow the registry of the 7 × 7 template. These clusters are decorated either on top of the first-layer Au clusters (upon the Au lattices) or at corner-hole sites. The former scenario can be simplified as a part of the conductive network; but the latter, as described above, forms stadiums. However, the number of these stadiums is insufficient to create detectable stable orbits and only leads to the loss of ergodicity. The corresponding differential conductance (yellow curve in Figure 5b) only exhibits gap shrinking. With increasing Au exposure, clusters tend to merge together and form Au islands (the upper STM image in Figure 5a). The differential conductance curves present not only a shrinking (even closing) gap but also two additional peaks at the vicinity of the band edges (arrows in Figure 5b). To clarify their origin, we make area statistics of the Au islands with the evolution of Au coverage, as shown in Figure 5c. The result of area distributions manifests two distinguishable peaks at each coverage, both of which can be fitted by Gaussian statistics. This indicates that two kinds of stadiums (A and B) exist during the growth. Given that the size of stadium B is nearly twice that of stadium A, the former probably originates from the merging of the latter. Since the evolution of the Au islands initially manifests quantitative growth then sized growth, the areas of stadiums A and B nonlinearly increase with Au exposure. The curve can be mathematically fitted to $\Omega = a\theta + b\theta^2$, where Ω is the area and θ is the Au coverage. The resonant states (i.e., eigenstates) in area Ω of the hexagon can be simply described by $E_n = E_0 + \lambda_n/$

DOI: 10.1021/acs.nanolett.7b04783
Nano Lett. XXXX, XXX, XXX−XXX

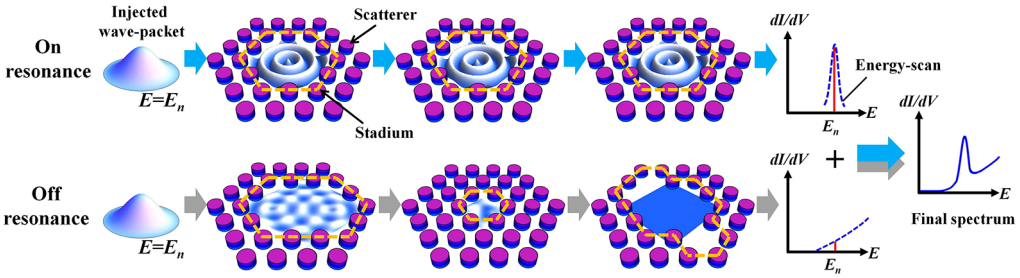

Figure 6. Schematic of stadium-induced resonant transport. The carrier denoted by a wave packet is injected with a well-defined energy (E_n). The conductance detected by another probe is shown in the right spectrum (red vertical line). If the energy is on-resonance, the injected carrier then mostly follows the stable orbit (as a resonance in that stadium), and the injected state can finally be well protected. If the energy is off-resonance, then the carrier undergoes chaotic scattering, finally showing a low conductance of background. The purple columns represent the corner-hole scatterers in a potential landscape, and the yellow polygons denote the figures of the stadiums formed in the array.

($m\Omega$) in atomic units, where E_n is the energy of eigenstates (n = 1, 2, 3..).[39] The energy onset E_0 = 0 and the effective mass ratio of the hole to electron (m_h^*/m_e^* = 0.903) are derived from the spectrum in Figure 4b. The fitting curves are shown in Figure 5d. The results indicate that the peaks in the spectrum in Figure 5b are closely related to the resonant states formed in stadium B, which corroborates our speculation that carrier transport can be modified by the controlled growth of the Au islands. Due to a larger area and more uniform statistical distribution of stadium B (fwhm is denoted by the error bar in Figure 5c), stable orbits for carrier transport preferentially form through stadium B rather than stadium A and then can be more easily and clearly observed in the conductance spectra. In some cases, the differential conductance spectrum shows only one resonant peak (instead of two, as shown in Figure 5b) either on the positive or negative bias range. However, the peak positions (labeled by crosses in Figure 5d) still follow the tendency of the fitting curve.

Such stadium-induced behavior is schematically described in Figure 6. If the energy of the injected carrier well matches the resonant condition (E_n) of, say stadium B, then stable orbits in each individual stadium form and even become dominant as "quantum scars"[35,37] in non-KAM dynamics. The injected carrier (shown as a wave packet) is expected to undergo less scattering in similar stadiums and behave as a resonant transport. Eventually, the resonant state can be well protected and is manifested as a high conductance in the dI/dV spectrum. For other stadiums (lower panel in Figure 6), the injected wave packet ($E = E_n$) is under the off-resonance condition of that stadium, which means it is in KAM dynamics. Carrier transport suffers chaotic scattering and then manifests background conductance that only presents the shrinking gap in the dI/dV spectrum. Such on- and off-resonances at different energies lead to the conductance spectra in Figure 5c; its evolution is obviously governed by the resonant states of the main stadiums (i.e., stadium B) under each Au coverage. These stadiums provide a "channel" on certain energies, where the traveling carrier undergoes fast transport and less loss. For some cases, the quantity of stadium B appearing on the electron propagation path is much different from that on the hole propagation path. The spectrum will present only one conductance peak at either the positive or negative bias range. Compared with the band-like transport in well-ordered 2DALs, the transport behavior controlled by coupled stadiums still lies on quantum chaotic dynamics but with regular phases, instead of with hyperbolic chaos. Similar effects can be found in a magnetic or/and electric field-driven system.[36,38,40] By contrast, in our work, the change from KAM to non-KAM dynamics is achieved and further controlled by the structural modification throughout a wide energy range as a tunable resonant transport. If the geometry of the scatterer array can be uniformly rearranged, such as using the template of 5 × 5 or 9 × 9 reconstruction, diverse long-range quantum transport phenomena are expected to be clearly observed and comprehensively studied. Such novel and well-ordered 2DALs with different periods and patterns will result in entirely different dynamics properties and even serve as a platform for studies on the quantum simulation of interacting many-body systems[41] and electronic quantum walks.[42]

In summary, we report a direct observation and control of quantum transport in artificial 2DALs, which are mainly governed by quantum chaotic dynamics and lattice symmetry. Low-temperature deposition produces 2DALs with a single-layer thickness, which largely suppresses the vertical electronic transport. A noninvasive double-probe STM/STS offers effective local transport control. Under this regime, the injected carrier is mainly constrained to 2D propagation and undergoes strong modulation in the 2DALs. In a well-ordered 2D structure, a periodic and compact arrangement of corner-hole vacancies acts as a scatterer array blocking the propagation of the injected carrier, which can be viewed as the confinement of a series of circular nested "quantum corrals" (as annual rings). The carrier appears being trapped and cannot escape from the "corrals" within a limited motion time and eventually exhibits an extremely low conductance as an energy gap in STS. By increasing the external electric field, the trapping is gradually broken down, and the escape probability increases to a detectable value. This escape probability obviously depends on the scatterer arrangement along the propagation direction, that is, the lattice symmetry, thereby resulting in a spatially anisotropic distribution. The transport behavior can be further modified by removing the scatterers in a well-ordered arrangement. With the controlled growth of the Au islands, a large number of stadiums can be constructed. Each stadium locally reforms the electronic states and induces the emergence of resonances (i.e., eigenstates), which can be viewed as several "atomic orbits" formed in a "super-atom" (or quantum dot). These "super-atoms" are distributed along the path of carrier propagation, couple together, and open a "channel" in the energy space where the carrier follows a stable orbit and undergoes less scatterings before escaping. This resonant transport can be triggered in a wide energy range, depending on the Au coverage we selected. Our findings would open the possibility of "quantum array" design and transport engineering,

DOI: 10.1021/acs.nanolett.7b04783
Nano Lett. XXXX, XXX, XXX−XXX

which is mainly governed by the scatterer arrangement and the dynamics property in a material system.

Experimental Section. The experiments were performed with a UHV system integrated with *RHK* multiprobe low-temperature STM and *Orsay* SEM. The multiprobe STM can be conducted in three operation modes: uniprobe STM mode, double-probe STM with all-contact mode, and double-probe STM/STS mode. *In situ* material deposition and cooling/heating (80−1500 K) were performed in a molecular beam epitaxy growth chamber. A clean and well-ordered 7 × 7 reconstructed surface on a *p*-type Si substrate (0.007 Ω cm) was first obtained with a well-established flash procedure and then cooled down to a liquid nitrogen temperature for examination. High-purity Au (99.9999%) was deposited on the cool Si(111)−7 × 7 template, achieving the low-temperature preparation of artificial 2DALs. The tungsten STM-tip used in the experiments was fabricated by electrochemical etching in KOH solution and subsequent cleaning by e-beam bombardment in UHV. Differential conductance was recorded under the open feedback condition by a lock-in amplifier (the *Signal Recovery* model 7265) with a modulation of 20 meV and with 1.987 kHz added to the bias voltage. All the measurements were performed at a cryogenic temperature of 77 K and a base pressure of 5×10^{-11} Torr.

■ ASSOCIATED CONTENT

Supporting Information

The Supporting Information is available free of charge on the ACS Publications website at DOI: 10.1021/acs.nanolett.7b04783.

Preparation of 2DALs with a single-layer thickness; noninvasive transport measurement with double-probe STM/STS; differential conductance measured at the double-layer 2DALs fabricated at room temperature; simulated current density distribution in double-probe STS configuration (PDF)

■ AUTHOR INFORMATION

Corresponding Authors

*E-mail: ypwu@xmu.edu.cn.
*E-mail: jykang@xmu.edu.cn.

ORCID

Kongyi Li: 0000-0003-1925-9808

Notes

The authors declare no competing financial interest.

■ ACKNOWLEDGMENTS

We would like to thank Ms. Li Chen, Mr. Mingming Fu, and Mr. Yihong Lu for their experimental assistance. This work was supported by the National Natural Science Foundation of China (Grant No. U1405253, 61674124, 11574257 and 11604275) and the Natural Science Foundation of Fujian Province of China (Grant No. 2018I01010026, 2014J01026, and 2017J01012).

■ REFERENCES

(1) Buluta, I.; Nori, F. Quantum Simulators. *Science* **2009**, *326* (5949), 108−111.
(2) Bartels, L. Tailoring molecular layers at metal surfaces. *Nat. Chem.* **2010**, *2* (2), 87−95.
(3) Polini, M.; Guinea, F.; Lewenstein, M.; Manoharan, H. C.; Pellegrini, V. Artificial honeycomb lattices for electrons, atoms and photons. *Nat. Nanotechnol.* **2013**, *8* (9), 625−633.
(4) Gomes, K. K.; Mar, W.; Ko, W.; Guinea, F.; Manoharan, H. C. Designer Dirac fermions and topological phases in molecular graphene. *Nature* **2012**, *483* (7389), 306−310.
(5) Sushkov, O. P.; Castro Neto, A. H. Topological Insulating States in Laterally Patterned Ordinary Semiconductors. *Phys. Rev. Lett.* **2013**, *110* (18), 186601.
(6) Guinea, F.; Katsnelson, M. I.; Geim, A. K. Energy gaps and a zero-field quantum Hall effect in graphene by strain engineering. *Nat. Phys.* **2010**, *6* (1), 30−33.
(7) Dean, C. R.; Wang, L.; Maher, P.; Forsythe, C.; Ghahari, F.; Gao, Y.; Katoch, J.; Ishigami, M.; Moon, P.; Koshino, M.; Taniguchi, T.; Watanabe, K.; Shepard, K. L.; Hone, J.; Kim, P. Hofstadter's butterfly and the fractal quantum Hall effect in moiré superlattices. *Nature* **2013**, *497* (7451), 598−602.
(8) Jiang, Y.; Zhang, Y. N.; Cao, J. X.; Wu, R. Q.; Ho, W. Real-Space Imaging of Kondo Screening in a Two-Dimensional O_2 Lattice. *Science* **2011**, *333* (6040), 324−328.
(9) Li, G.; Höpfner, P.; Schäfer, J.; Blumenstein, C.; Meyer, S.; Bostwick, A.; Rotenberg, E.; Claessen, R.; Hanke, W. Magnetic order in a frustrated two-dimensional atom lattice at a semiconductor surface. *Nat. Commun.* **2013**, *4*, 1620.
(10) Zhang, C.; Wu, Y.; Zhou, Y.; Gao, N.; Guo, F.; Chen, X.; Jiang, B.; Hu, W.; Kang, J. Two-dimensional Au lattices featuring unique carrier transport preference and wide forbidden gap. *Nanoscale* **2014**, *6* (17), 10118.
(11) Ji, S.-H.; Hannon, J. B.; Tromp, R. M.; Perebeinos, V.; Tersoff, J.; Ross, F. M. Atomic-scale transport in epitaxial graphene. *Nat. Mater.* **2011**, *11* (2), 114−119.
(12) Sutter, P. W.; Flege, J.-I.; Sutter, E. a. Epitaxial graphene on ruthenium. *Nat. Mater.* **2008**, *7* (5), 406−411.
(13) Nakayama, T.; Kubo, O.; Shingaya, Y.; Higuchi, S.; Hasegawa, T.; Jiang, C.-S.; Okuda, T.; Kuwahara, Y.; Takami, K.; Aono, M. Development and Application of Multiple-Probe Scanning Probe Microscopes. *Adv. Mater.* **2012**, *24* (13), 1675−1692.
(14) Li, A.-P.; Clark, K. W.; Zhang, X.-G.; Baddorf, A. P. Electron Transport at the Nanometer-Scale Spatially Revealed by Four-Probe Scanning Tunneling Microscopy. *Adv. Funct. Mater.* **2013**, *23* (20), 2509−2524.
(15) Zhang, T.; Cheng, P.; Li, W.-J.; Sun, Y.-J.; Wang, G.; Zhu, X.-G.; He, K.; Wang, L.; Ma, X.; Chen, X.; Wang, Y.; Liu, Y.; Lin, H.-Q.; Jia, J.-F.; Xue, Q.-K. Superconductivity in one-atomic-layer metal films grown on Si(111). *Nat. Phys.* **2010**, *6* (2), 104−108.
(16) Shchukin, V. A.; Ledentsov, N. N.; Bimberg, D. *Epitaxy of Nanostructures*; Springer Science & Business Media, 2013.
(17) Köhler, U. Scanning tunneling microscopy study of low-temperature epitaxial growth of silicon on Si(111)-(7 × 7). *J. Vac. Sci. Technol., A* **1989**, *7* (4), 2860.
(18) Won, H.; Willis, R. F. A STM point-probe method for measuring sheet resistance of ultrathin metallic films on semiconducting silicon. *Surf. Sci.* **2010**, *604* (5−6), 490−494.
(19) Armstrong, J. N.; Hua, S. Z.; Chopra, H. D. Strength of metals at the Fermi length scale. *Phys. Status Solidi RRL* **2012**, *6* (3), 99−101.
(20) Heller, E. J.; Crommie, M. F.; Lutz, C. P.; Eigler, D. M. Scattering and absorption of surface electron waves in quantum corrals. *Nature* **1994**, *369* (6480), 464−466.
(21) Jeandupeux, O.; Bürgi, L.; Hirstein, A.; Brune, H.; Kern, K. Thermal damping of quantum interference patterns of surface-state electrons. *Phys. Rev. B: Condens. Matter Mater. Phys.* **1999**, *59* (24), 15926−15934.
(22) Vance, W. N. Unstable periodic orbits and transport properties of nonequilibrium steady states. *Phys. Rev. Lett.* **1992**, *69* (9), 1356−1359.
(23) Lloyd, J.; Rondoni, L.; Morriss, G. P. Breakdown of ergodic behavior in the Lorentz gas. *Phys. Rev. E: Stat. Phys., Plasmas, Fluids, Relat. Interdiscip. Top.* **1994**, *50* (5), 3416−3421.

DOI: 10.1021/acs.nanolett.7b04783
Nano Lett. XXXX, XXX, XXX−XXX

(24) Yoshimura, M.; Kirkpatrick, T. R. Long-range correlations in nonequilibrium quantum Lorentz gases. *Phys. Rev. B: Condens. Matter Mater. Phys.* **1996**, *54* (10), 7109−7120.
(25) Lloyd, J.; Niemeyer, M.; Rondoni, L.; Morriss, G. P. The nonequilibrium Lorentz gas. *Chaos* **1995**, *5* (3), 536.
(26) Odbadrakh, H.; Morriss, G. P. Nonhyperbolic behavior in the thermostated Lorentz gas. *Phys. Rev. E: Stat. Phys., Plasmas, Fluids, Relat. Interdiscip. Top.* **1999**, *60* (4), 4021−4026.
(27) Schmiedeberg, M.; Stark, H. Superdiffusion in a honeycomb billiard. *Phys. Rev. E* **2006**, *73* (3), 31113.
(28) Mucciolo, E. R.; Capaz, R. B.; Altshuler, B. L.; Joannopoulos, J. D. Manifestation of quantum chaos in electronic band structures. *Phys. Rev. B: Condens. Matter Mater. Phys.* **1994**, *50* (12), 8245−8251.
(29) Lobo-Checa, J.; Matena, M.; Muller, K.; Dil, J. H.; Meier, F.; Gade, L. H.; Jung, T. A.; Stohr, M. Band Formation from Coupled Quantum Dots Formed by a Nanoporous Network on a Copper Surface. *Science* **2009**, *325* (5938), 300−303.
(30) Kagan, C. R.; Murray, C. B. Charge transport in strongly coupled quantum dot solids. *Nat. Nanotechnol.* **2015**, *10* (12), 1013−1026.
(31) Clark, K. W.; Zhang, X.; Vlassiouk, I. V.; He, G.; Feenstra, R. M.; Li, A.-P. Spatially Resolved Mapping of Electrical Conductivity across Individual Domain (Grain) Boundaries in Graphene. *ACS Nano* **2013**, *7* (9), 7956−7966.
(32) Kliewer, J.; Berndt, R.; Crampin, S. Controlled Modification of Individual Adsorbate Electronic Structure. *Phys. Rev. Lett.* **2000**, *85* (23), 4936−4939.
(33) Bleher, S.; Ott, E.; Grebogi, C. Routes to chaotic scattering. *Phys. Rev. Lett.* **1989**, *63* (9), 919−922.
(34) Ding, M.; Grebogi, C.; Ott, E.; Yorke, J. A. Transition to chaotic scattering. *Phys. Rev. A: At., Mol., Opt. Phys.* **1990**, *42* (12), 7025−7040.
(35) Gutzwiller, M. C. *Chaos in Classical and Quantum Mechanics*; Springer: New York, 1990.
(36) Brunner, R.; Meisels, R.; Kuchar, F.; Akis, R.; Ferry, D. K.; Bird, J. P. Draining of the Sea of Chaos: Role of Resonant Transmission and Reflection in an Array of Billiards. *Phys. Rev. Lett.* **2007**, *98* (20), 204101.
(37) Wilkinson, P. B.; Fromhold, T. M.; Eaves, L.; Sheard, F. W.; Miura, N.; Takamasu, T. Observation of 'scarred' wavefunctions in a quantum well with chaotic electron dynamics. *Nature* **1996**, *380* (6575), 608−610.
(38) Fromhold, T. M.; Patanè, A.; Bujkiewicz, S.; Wilkinson, P. B.; Fowler, D.; Sherwood, D.; Stapleton, S. P.; Krokhin, a a; Eaves, L.; Henini, M.; Sankeshwar, N. S.; Sheard, F. W. Chaotic electron diffusion through stochastic webs enhances current flow in superlattices. *Nature* **2004**, *428* (6984), 726−730.
(39) Li, J.; Schneider, W.-D.; Berndt, R.; Crampin, S. Electron Confinement to Nanoscale Ag Islands on Ag(111): A Quantitative Study. *Phys. Rev. Lett.* **1998**, *80* (15), 3332−3335.
(40) Fromhold, T. M.; Wilkinson, P. B.; Hayden, R. K.; Eaves, L.; Sheard, F. W.; Miura, N.; Henini, M. Tunneling spectroscopy of mixed stable-chaotic electron dynamics in a quantum well. *Phys. Rev. B: Condens. Matter Mater. Phys.* **2002**, *65* (15), 155312.
(41) Bloch, I.; Dalibard, J.; Nascimbène, S. Quantum simulations with ultracold quantum gases. *Nat. Phys.* **2012**, *8* (4), 267−276.
(42) Genske, M.; Alt, W.; Steffen, A.; Werner, A. H.; Werner, R. F.; Meschede, D.; Alberti, A. Electric Quantum Walks with Individual Atoms. *Phys. Rev. Lett.* **2013**, *110* (19), 190601.

DOI: 10.1021/acs.nanolett.7b04783
Nano Lett. XXXX, XXX, XXX−XXX